Icarus **152**, 366–383 (2001)
doi:10.1006/icar.2001.6645, available online at http://www.idealibrary.com on IDEAL®

AAT Observations of the SL9 Fragment C, D, G, K, N, R, V, and W Impacts with Jupiter: Lightcurves and Imaging

Victoria Meadows and David Crisp

MS183-900, Jet Propulsion Laboratory/California Institute of Technology, 4800 Oak Grove Drive, Pasadena, California 91109
E-mail: vsm@hesperos.jpl.nasa.gov

Jason Barnes[1]

Astronomy Department, MS105-24, California Institute of Technology, Pasadena, California 91125

Glenn Orton

MS169-237, Jet Propulsion Laboratory/California Institute of Technology, 4800 Oak Grove Drive, Pasadena, California 91109

and

John Spencer

Lowell Observatory, 1400 West Mars Hill Road, Flagstaff, Arizona 86001

Received June 8, 2000; revised March 5, 2001

We used the InfraRed Imaging Spectrometer (IRIS) on the Anglo-Australian Telescope to monitor the July 1994 impacts of Comet Shoemaker–Levy 9 with Jupiter. Spectral image cubes were obtained for the impacts of fragments C, D, G, K, R, and W. These data provide time sequences of spatially resolved spectra in K-band (1.98 to 2.40 μm), with a spectral resolution of 300 ($\lambda/\Delta\lambda$) and a spatial sampling of 0.6 arcsec/pixel. Fast-rate 2.35-μm filter photometry was used to monitor the impacts of fragments N and V. Our imaging and spectral observations track the entire evolution of each impact, from the time the fragment entered the jovian atmosphere, until the impact site rotates into view. In this paper, we concentrate on photometry and imaging results. We present photometrically calibrated lightcurves for seven impacts, and an estimate of the peak brightness for the V impact. Each event we observed, with the exception of V, was first detected as a faint "precursor," which was followed 5–10 min later by a much brighter "main event." Precursor flashes for fragments G and K were first recorded about 30 and 90 s before an impact event was detected by instruments on the *Galileo* spacecraft. The precursor for the N impact was seen in our data 4 s before detection by the *Galileo* SSI, but may have occurred up to 30 s earlier due to gaps in our time sampling. The steady initial brightening of the lightcurves for fragments G and K indicates that these impacts may have been preceded by infalling dust. A radiative transfer model was used to determine the minimum vertical altitude at which the incoming meteor would have been directly visible to ground-based observers. The results indicate that the first precursor is most likely due to detection of impacting dust from each fragment's coma, rather than a bolide produced by the fragment itself. The onset of the main event and the first detection of high-temperature CO occur at times that are not a function of impactor energy. However, the time to reach peak brightness in the NIR lightcurves is a strong function of impactor energy, with lowest to highest energy impactors (N to K) taking from 2 to 8 min to reach peak flux after the onset of the main event. Very different peak impact brightnesses were found when comparing fragments from the main comet train with fragments with similar preimpact brightnesses that had been observed to travel displaced from the main train. These differences indicate compositional or structural differences between these two families of fragments.

Key Words: **comets, SL9; Jupiter; impact processes; infrared observations; photometry.**

1. INTRODUCTION

Between 15 and 22 July, 1994, more than 20 fragments of Comet Shoemaker–Levy 9 (SL9) collided with Jupiter. These multiple collisions provided the first opportunity to observe a major Solar System impact event with modern astronomical instruments. Although the impacts occurred on the far side of Jupiter, just beyond the morning limb, observations of the event were made by almost every major ground-based telescope, the Hubble Space Telescope, and the *Galileo* spacecraft. To monitor this event we used the InfraRed Imaging Spectrometer

[1] Current address: Lunar and Planetary Laboratory, University of Arizona, 1629 E. University Blvd., Tucson, AZ 85721.

0019-1035/01 $35.00

(IRIS) on the 3.9-m Anglo-Australian Telescope (AAT) at Siding Spring Observatory, near Coonabarabran, Australia. This southern hemisphere site, and excellent observing conditions over 8 nights, allowed us to obtain data on the impacts of the comet fragments that had been labeled C, D, G, K, N, R, V, and W. This paper describes the observations and provides timing and photometric lightcurves for the impact events. Discussion of the fully calibrated spectral sequences, characteristics of the precursor spectra, and preliminary spectral modeling results, including identification of observed emitting species, can be found in Paper 2 (Meadows *et al.*, 2001, in prep).

The SL9 fragments were all predicted to enter the atmosphere of Jupiter near 45° South latitude, about 8° beyond the morning limb of Jupiter (Chodas and Yeomans 1994 (e-mail predictions), later published in Chodas and Yeomans 1996). Consequently the impact points were not directly visible to Earth-based observers (ground-based and HST). The viewing geometry was more favorable for the *Galileo* spacecraft, which was on its way to Jupiter and able to image the impact sites directly. Although it was not expected that ground-based and HST observers would be able to see any of the impact phenomena directly, the proximity of the impact points to the morning limb meant that the fresh impact sites would rotate into Earth view in less than 20 min. However, ultimately both ground-based observers and the HST saw phenomena prior to, during, and after the impacts. Timing and photometric information from various sources, including direct observations of the impacts by the *Galileo* spacecraft, were combined to produce the following plausible scenario for the timeline of the impacts (see Chapman (1996) for a more detailed description).

As a comet fragment's coma and then its nucleus entered the upper jovian atmosphere, the atmosphere was heated, producing a warm meteor trail. This trail was believed to be high in the atmosphere where it could be seen by ground-based near-infrared observers. Initially the ground-based detection of the faint SL9 impact meteor activity produced a great deal of confusion amongst the planetary observing community, as ground-based observers apparently "saw" the impact beyond the limb, before *Galileo* detected it from its superior vantage point above the impact site. It was initially thought that this meteor or bolide phenomenon was detected by ground-based observers but was not detected by the *Galileo* spacecraft because of the larger collecting areas of ground-based telescopes and higher sensitivities from ground-based instrumentation (Orton *et al.* 1995, Martin *et al.* 1995). However, Chapman argues that the single event detected by the *Galileo* instruments contained this bolide event as the first few seconds of the phenomenon (Chapman 1996). Before its origin was known, this meteor activity was given the name "first precursor." Once the fragment entered the jovian atmosphere it reached a terminal altitude and exploded, sending impact ejecta back up the incoming shock tube and out as an expanding plume of hot gas and particulates. The upper parts of the bolide trail may have also exploded to produce the upper portion of the fireball (Boslough *et al.* 1994, 1995). The terminal explosion and ensuing initial fireball were observed by the *Galileo* spacecraft, and thermal emission from the expanding plume was observed at visible and near-infrared wavelengths by HST and ground-based telescopes once it had risen a sufficient distance above the jovian atmosphere. This expanding, cooling plume phase was dubbed "the second precursor." As the plume expanded and cooled, material rained back down onto Jupiter, shocking the atmosphere and producing the brightest of all the observed phenomena at infrared wavelengths, the so-called "main event," or "splash." As the impact site rotated onto the Earth-facing hemisphere, the impact debris appeared as a bright feature at near-infrared wavelengths, and a dark feature at most visible wavelengths.

2. OBSERVATIONS

IRIS is a near-infrared camera/spectrometer with a 128×128 HgCdTe (NICMOS2) detector. It can be used for direct imaging at wavelengths between 0.9 and 2.5 μm, or for spatially resolved near-infrared slit spectroscopy of extended objects (see Allen *et al.* (1993) for a detailed description of the instrument). To monitor the SL9 impact events, IRIS was used primarily as an imaging spectrometer, and was configured to provide spatially resolved spectra with a spectral resolution of $\lambda/\Delta\lambda \sim 300$, and a spatial sampling of 0.6″/pixel. Time resolved K-band (1.98–2.4 μm) image cubes were recorded during the impacts of fragments C, D, G, K, R, and W. Some H-band (1.4–1.8 μm) image cubes were also obtained during these impacts. Imaging photometry with a 2.34-μm filter was used to monitor the impacts of fragments N and V. We also acquired H- and K-band spectral image cubes of the impact sites for up to 10 h each day during the week of the impacts.

The spectral image cubes were compiled by scanning the telescope across the jovian disk perpendicular to the $60'' \times 1''$ slit, while recording spectra at slit positions separated by 0.6 arcsec. The slit was aligned with the jovian equator. The telescope was programmed to scan from south to north, and then from north to south across the jovian disk. Spatial information was recorded along both the slit length and drift direction, producing a 2-dimensional image, while simultaneously recording a spectrum for each pixel in the image. These data can be organized to produce a 3D cube with two spatial dimensions and one spectral dimension (Fig. 1). With a 1.5-s sampling time at each slit position, a complete image of the jovian disk can be produced in about two minutes. For the majority of the impacts, this is our time resolution. However, a smaller scan distance was used to monitor the impacts of fragments C and K. For these impacts only a small region around the impact latitude was imaged, increasing the time resolution to approximately 30–40 s between scans. For the impact of fragment K, this small area allowed higher time resolution to monitor a possible flash from the impact reflected off the jovian satellite Europa, which was in Jupiter's shadow, but visible from Earth at the predicted time of the K impact. In an attempt to avoid saturation of the detector during the impacts, the

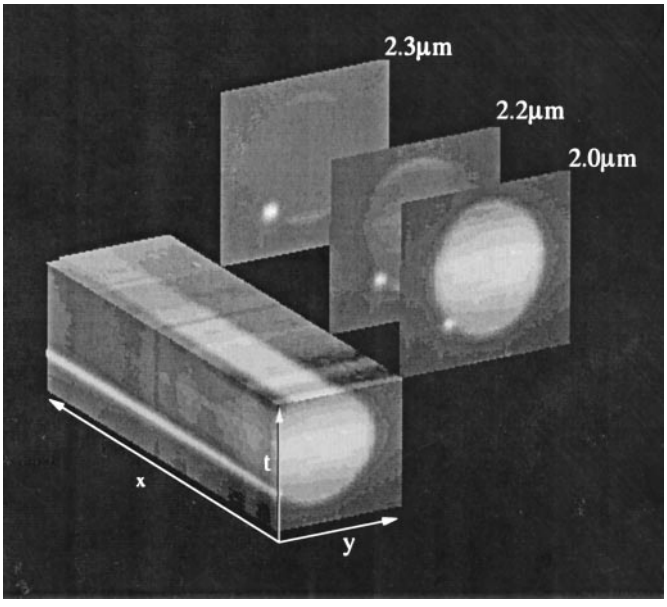

FIG. 1. Representation of an IRIS data cube. These data were taken at 07:38 UT on 18 July during the G impact. The *y* axis shows the orientation of the spectometer slit, which ran parallel to the jovian equator. Spectra were dispersed orthogonal to the slit in the *x* direction. The origin of the *x* axis is at 1.98 μm, and it increases toward 2.4 μm at the back of the cube. To acquire the spectral-imaging cube, the slit was scanned perpendicular to the jovian equator in the *t*, or scan direction. Three images (*yt* planes) extracted from the full cube at 2.0 μm (front), 2.2 μm (middle), and 2.3 μm (back) are shown for comparison. The cube has also been sliced in *xt* to reveal one of the planes containing the spectrum of the G impact main event, which can be seen as a bright streak on the side of the cube. The top surface of the cube is an *xy* plane that shows a spectrum of Jupiter's northern latitudes and the adjacent sky.

AAT mirror cover was partially closed for the brightest portions of the impact events. This approach was largely successful, but necessitated additional calibration steps to recover the absolute brightness of these events.

Due to the anticipated smaller size of the N and V fragments, we used fast-rate photometry, rather than spectral imaging, to observe these impacts. For the N impact, we configured the instrument to take 100 successive imaging observations of 0.45 s exposure time, before dumping the resultant image cube to disk, a process which took approximately 25 s. The N data set therefore consists of successive observations of 45 s of fast-rate photometry, interspersed with data gaps of 25 s. Just after the peak of the impact we experienced an instrument failure, but regained data acquisition capabilities within four minutes.

For the impact of fragment V, there was some concern that the impact would be so small, and the phenomena so short-lived, that it would be lost entirely if it occurred while an image cube was being recorded to disk. Consequently, we configured IRIS in the safer but less efficient repeat mode, where single exposures of 0.45 s were read out continuously, with a deadtime of 6 s between each exposure. We observed in this mode from 22 July 04:02:45 UT until 04:40:26 UT. Even though we detected no impact phenomena in real time, the V impact event was later found in the processed data. Table I summarizes the observing times and observing mode used for each day of observation, and Fig. 2 shows images near peak brightness for each impact we observed.

2.1. Data Reduction

All IRIS data were first corrected for the nonlinear response of the HgCdTe detector to incident radiation. For the spectral imaging data, standard spectral reduction techniques were then applied to each spectral plane of the datacubes to remove instrument response. Flatfield observations of a uniform source illuminating a white patch of the telescope dome were used to correct for the spectral and spatial response of the detector. After flatfielding, bad pixels were removed by interpolation. For spectral-imaging observations, distortions in the curvature of the grism order were corrected with polynomial fits. The effect of the apparent rotation of the slit along the spectrum was also characterized and corrected. After completing these steps, the instrumental artifacts in the data had been largely removed.

The next processing step involved removing sky emission and transmission effects from the data. To correct for the underlying emission from the sky, scan (t) positions in the datacube were found where the spectrometer slit was sampling only background sky, thereby producing a set of 2D sky spectra in the *xy* plane (see Fig. 1). These *xy* planes were then averaged to form a composite sky frame, and subtracted from all *xy* planes of the data. This step corrected for not only the spectral behavior of the sky, but pixel-to-pixel bias variations on the detector in the *y* (slit) direction. To account for the time-varying brightness of the sky during the duration of the scan back and forth across the planet, *xt* planes were selected near the ends of the slit, which contained only sky emission. An averaged *xt* plane of the time-dependent sky brightness was produced, and subtracted from each *xt* plane in the previously *xy* plane sky-subtracted cube.

After removal of sky emission, the effect on the observed spectrum due to wavelength-dependent sky transmission was removed. In preparation for this step, a wavelength scale in mi-

TABLE I
Summary of AAT K-Band Observations

Date (UT) (July)	Start obs. (UT)	End obs. (UT)	Impact	Observing mode	λ range (μm)	Airmass
16	9:25	12:50	—	Driftscan	2.0–2.4	—
17	4:40	11:10	C	Driftscan	2.0–2.4	1.10
17	11:10	13:45	D	Driftscan	2.0–2.4	1.59
18	5:50	13:45	G	Driftscan	2.0–2.4	1.09
19	5:45	13:20	K	Driftscan	2.0–2.4	1.24
20	6:35	12:45	N	Imaging	2.34	1.17
21	4:35	13:00	R	Driftscan	2.0–2.4	1.33
22	3:45	4:40	V	Imaging	2.34	1.84
22	4:40	12:40	W	Driftscan	2.0–2.4	1.06
23	8:15	12:50	—	Driftscan	2.0–2.4	—

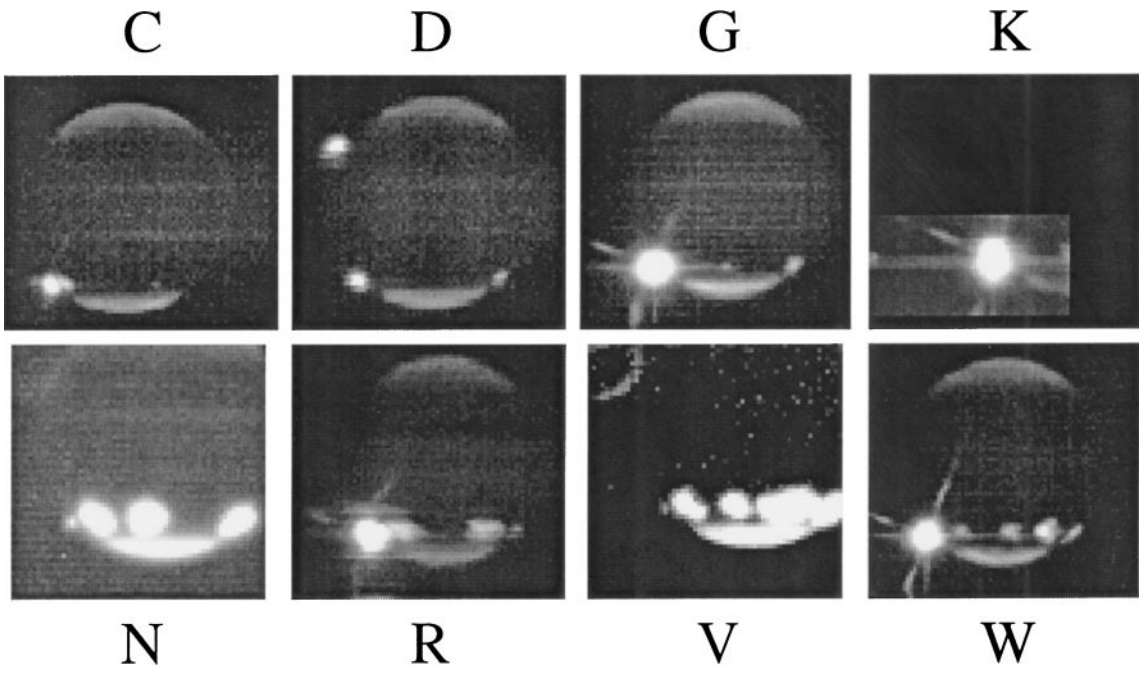

FIG. 2. The AAT SL9 impact "Family Portrait," providing morphological overview images taken near peak brightness for each impact observed at the AAT. These images are not photometrically calibrated, and only rough relative brightnesses are shown in this diagram. Images for C, D, G, K, R, and W have been sliced from spectral mapping cubes in the wavelength range 2.32–2.38 μm, whereas the images from N and V were taken through a CO 4% filter (effective bandpass 2.32–2.38 μm). In this wavelength range Jupiter appears dark due to strong absorption of sunlight by methane in its upper atmosphere. However, scattering of sunlight by aerosols high in the atmosphere above the absorbing methane can be seen in the north and south polar regions. Each impact can be seen as a bright source at -45° latitude on the morning limb of the planet (the left-hand side in the images). Previous impacts leave large areas of scattering particulates above the methane and can be seen as bright oval to irregular sources across the jovian disk at -45° latitude. These old impact sites persisted throughout and well beyond the impact week, causing this latitude band to becomes more populated with these features with each successive impact.

crometers was derived from observations of arc lamps taken with the instrument in the observing configuration. This arc-derived wavelength fit is added to the x axis of the data. The data were then divided by a wavelength-calibrated standard star spectrum observed with the same optical configuration, and at a similar zenith distance (altitude) to the data. The slope in the infrared spectrum introduced by the temperature of the standard star was modeled using a blackbody curve and removed from the data.

The fast-rate photometric imaging data for the impacts of fragments N and V were processed using standard near-infrared reduction techniques, including linearization, flatfielding, interpolation of bad pixels, and sky-subtraction.

2.2. Calibration

Absolute calibration of the SL9 spectral mapping cubes was challenging. Observations of spectrophotometric standard stars were taken on the same nights as the data, with the same instrument configuration used to observe Jupiter, including a $1''$ wide slit. However, as the slit was comparable in width to the seeing profile (which was $1''$ FWHM on most nights, but deteriorated episodically to as much as $6''$ FWHM), it contained too little of the light from the standard star to produce consistent photometric measurements (variations of up to a factor of 3 were found in the total flux for the same star observed at different times on the same night), and therefore could not be used for spectrophotometry. Also, to avoid saturating at the peak of the brightest impacts, the mirror was actively stopped down over several minutes of data-taking in a manner that made it difficult to reproduce while observing a standard star. Observations were also taken starting in the early afternoon and continuing through the night, with correspondingly large variations in sky conditions. Consequently the standards were used principally for correcting for atmospheric transmission effects in the data, as described in the previous section, and not for absolute photometric calibration.

Looking for alternate methods of absolute calibration, we investigated using Galilean satellites, polar haze, and imaging photometric standard stars. The final calibration method combined all three types of measurements. We used the photometric standards and the jovian satellites as two independent means of calibrating the polar haze in samples of both the imaging and the spectral mapping data, and then used this pole calibration to calibrate the remaining data. A jovian pole was included in almost all of our imaging and spectroscopic data, and monitoring the polar brightness allowed us to correct for rapid and otherwise nonquantifiable changes in the effective aperture of the telescope (the mirror cover on the 3.9-m AAT was partially closed during the brightest impact flashes to prevent saturation of the detector).

However, before the poles could be used to calibrate the observations, we had to accurately determine their brightness, and verify that it was stable and not altered appreciably by auroral emission. This process is described in the following three subsections.

2.2.1. Absolute calibration of the jovian poles. To provide an absolute calibration for the jovian poles, we used data taken on 21 July 1994. These data included spectral mapping cubes that contained both poles of Jupiter and the Galilean satellite Io, and also imaging data containing the south pole of Jupiter. An image plane containing Io and both poles of Jupiter was extracted from a spectral mapping cube in the wavelength range 2.32–2.38 μm. This region was chosen to mimic the filter bandpass for the 2.34-μm CO imaging data. Using albedos derived from Sill and Clark (1982), and the World Meteorological Organization solar spectrum (Wehrli 1986) we calculated the flux of Io in this wavelength range to be 7.9×10^{-12} W m^{-2} μm^{-1}. Large rectangular apertures that included the entire haze-covered north and south polar regions were used to obtain values of 1.2–1.4 $\times$ 10^{-12} W m^{-2} μm^{-1} for both poles in the spectral imaging data. To check this value, we measured the polar brightness in the imaging data, which was calibrated using imaging photometric standards taken at the beginning of the observing run with the 2.34-μm narrowband (4% bandpass) filter. These standards were observed in a $19'' \times 19''$ aperture that contained more than 99% of the light from the star (HD129540, an A2V; Carter and Meadows 1995). Given the star's K (2.2 μm) magnitude, and assuming negligible magnitude color difference for an A2V star between 2.2 and 2.34 μm, the south pole in several frames of the N imaging data was found to have a brightness of 1.2–1.3 $\times$ 10^{-12} W m^{-2} μm^{-1}. Consequently, a value of $1.3 \pm 0.1 \times 10^{-12}$ W m^{-2} μm^{-1} was adopted for the brightness of each jovian pole.

This independently derived calibration has subsequently been cross-checked using the jovian absolute reflectivity spectra provided in Chanover *et al.* (1996). Our calibration for the brightness of the jovian south pole at 2.34 μm on UT 18 Jul agrees to within 5–10% of the Chanover-derived values, which is well within measurement errors.

2.2.2. Errors and uncertainties in calibration. The AAT observations of the SL9 impacts were taken under photometric conditions. However, using a narrow slit to spectrally image a point source (or an unresolved area associated with an impact event) introduces errors that compromise photometric accuracy. As the narrow slit is stepped across the object, variations in seeing produce a time-varying point-spread function (PSF) that changes in both FWHM and spatial position. These changes make it almost impossible to correctly sample the object's PSF. This effect can be ameliorated by taking several scans back and forth across the object to average the effects of the seeing. However, for the rapidly changing phenomena associated with the impact events, this was not possible, as subsequent scans showed very different phenomena, and could not be averaged. To quantify the error associated with this effect a nonvariable point source observed simultaneously with the data is required. For the majority of the spectral mapping data, this source was best provided by the Galilean satellites. Although the satellities are not point sources, their angular size is sufficiently small (ranging from $1.0''$ for Io to $1.4''$ for Ganymede) that it is comparable to the seeing disk. Performing aperture photometry on images of the Galilean satellites extracted from the spectral mapping cubes produced the standard deviations in measured counts shown in Table II. This error is correlated with the seeing, being larger on nights of poorer seeing (21 July produced the largest median seeing). However, when the satellite observations within a given night are averaged, absolute fluxes derived for the same satellite observed on different nights showed a standard deviation of 12% for Europa, which was observed on 17, 19, and 21 July. If measurements taken only on 17 and 19 July are considered, this discrepancy falls to 3%. The standard deviation for Io, which was observed on 19 and 21 July, was 1%.

TABLE II
Photometric Errors for Drift Scan Observations of the Galilean Satellites

UT date	Satellite	Std. dev. (%)
17 Jul	Europa	15
19 Jul	Europa	8
19 Jul	Io	5
21 Jul	Europa	23
21 Jul	Io	10
22 Jul	Ganymede	5

2.2.3. The stability of polar haze measurements. To estimate the error introduced by using the large aperture measurement of the brightness of the polar haze as a calibration source, we first corrected for airmass by plotting measurements of north pole brightness in the wavelength range 2.32 to 2.38 μm (to approximate the standard CO imaging filter) as a function of airmass. We typically derived an extinction coefficient at K-band of approximately -0.10 mags/airmass. This is consistent with accepted values for the extinction at this site (David Allen, private communication, 1993). For all five nights in which imaging spectroscopy was taken, this relationship was fit with a straight line with a typical standard deviation of 5% (21 July gave a standard deviation of 7%). These results indicate that the intrinsic relative variability of the pole on any given night is actually quite low (5–7%) over this wavelength range.

Another possible complication in using the polar haze measurements as a calibration source is the systematic enhancement of the polar haze intensity by impact-induced auroral activity. Bright impact-induced auroral emission, such as that seen in WFPC2 UV images (Clarke *et al.* 1995) and at near-infrared wavelengths (McGregor *et al.* 1996), was fixed in a narrow longitude range, i.e., with a small spatial extent compared with the bright polar haze region. This fixed-longitude auroral enhancement would be expected to rotate with the planet, producing

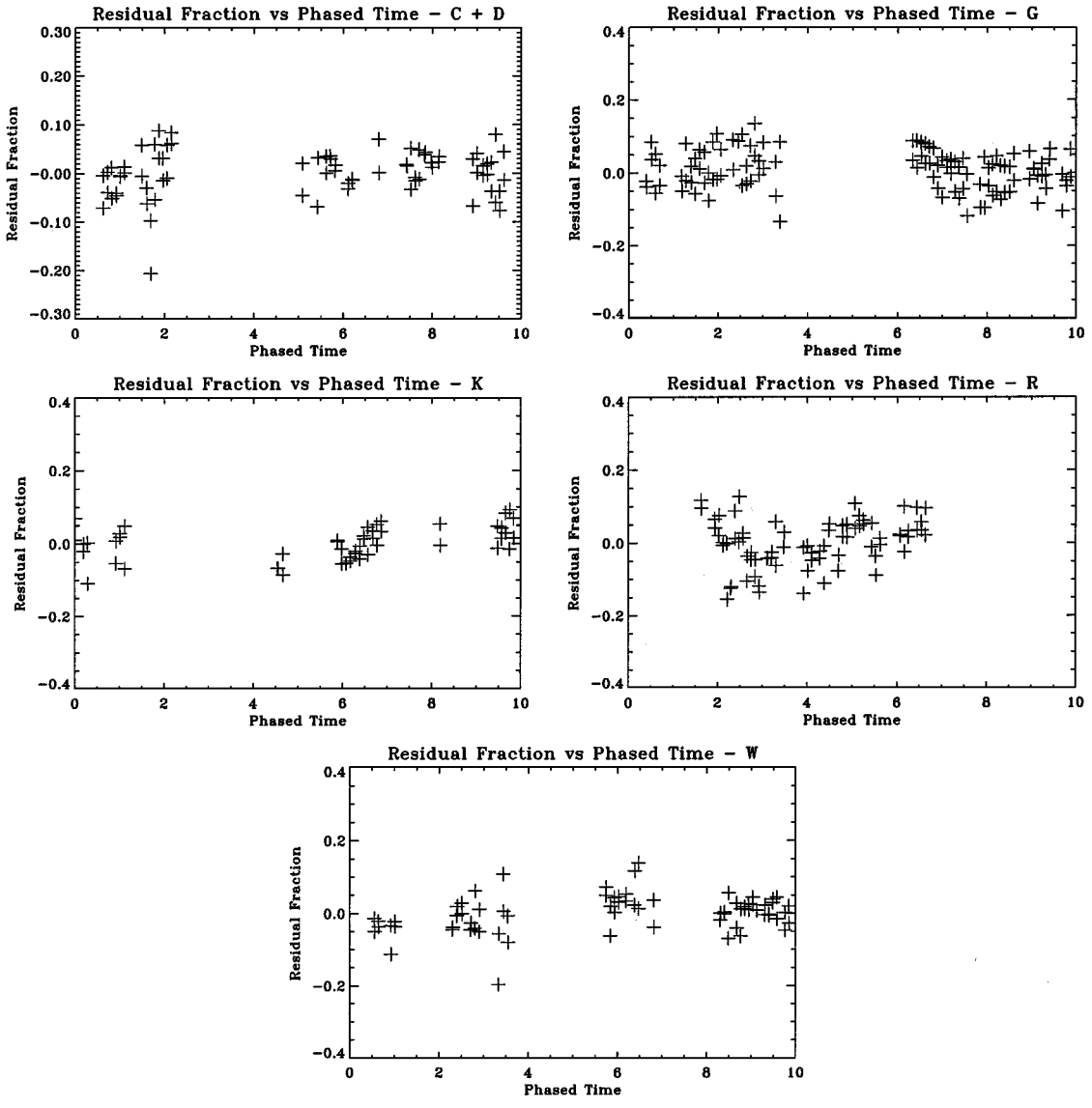

FIG. 3. Plots of residual north pole counts (after removal of the straight-line fit to correct for airmass) as a fraction of total counts in the aperture, as a function of phased time (with 0:00 time set as 00:00 h 16 July 1994, and assuming a jovian rotation period of 9.925 h). No obvious enhancement of the observed emission as a function of phased time (longitude) in this wavelength range is seen.

a brightness enhancement to the polar emission that varied with rotational phase. To search for this possible effect, we plotted north pole count residuals (after subtraction of the airmass fit for each night) as a function of phased time. Points observed at the same phased time have approximately the same longitude on the planet. The results show no obvious enhancement of the observed emission as a function of longitude in this wavelength range (Fig. 3), and appear to confirm that the polar brightness was sufficiently stable at these wavelengths to use for calibration. This apparent stability is probably due to significant "dilution" of any spatially localized, narrow-line auroral enhancement within the large spatial and spectral (2.32 to 2.38 μm) measurement aperture used here to determine the brightness of the polar haze.

The final reduced and calibrated data for the impacts were archived in the Atmospheres Node of the Planetary Data System in April 1998 (Meadows *et al.* 1998).

2.3. Measurement of Lightcurves

2.3.1. Spectral-imaging data. The accuracy of the lightcurve photometry will depend not only on the absolute calibration of the data, but also on the measurement aperture size and shape used to determine the integrated intensity of the impact events. A small circular aperture was used to measure the initial stages of the impact phenomena, when the impact emission was point-like. This small measurement aperture minimized contamination of the measurement by background planetary emission

(which is a relatively small component at CO filter wavelengths, 2.32–2.38 μm), and by emission from nearby older impact sites. The latter effect is a much larger contaminant, and can vary as scattered light from companion impact sites flares into the measurement aperture in poor seeing. The total emission from the impact was estimated by measuring the impact at or near its peak brightness to determine the fraction of the radiation observed in the small measurement aperture compared to the "total" emission in a much larger aperture. This "aperture correction" is determined near peak brightness so that contamination in the larger measurement aperture by scattered light from nearby impact sites and the underlying planet will be a very small component of the impact emission, even in the far wings of the PSF. Once determined from the brightest possible observations, the aperture correction was then applied to measurements made with a smaller aperture during the fainter stages of the impact.

However, a small circular aperture could not be used much after peak brightness. By that time, the observed emission became extended as the impact site started to rotate into view over the morning limb. A larger measurement aperture was therefore used, to encompass most of the light from the extended impact site. However, in doing so, the possibility of contamination by emission from the underlying planet and nearby impact sites was greatly increased.

The D, G, and K impacts did not occur close to a previous large impact site. For these impacts, measurements were initially made using a 1.8″ (3 pixel) radius circular aperture, which was corrected to a 4.2″ (7 pixel) radius aperture based on measurements made near peak brightness for each impact. This aperture correction typically added 15–20% to the 1.8″ measurement. For the D impact, the impact site was sufficiently small that it never appeared resolved in our images, so all points on the D lightcurve are 1.8″ measurements corrected to 4.2″ radius apertures. For G and K, the impact sites were resolved at approximately UT 7:44 (18 July) and UT 10:36 (19 July) respectively. At peak brightness at 7:46 UT (18 July) a slice taken tangent to the limb through the G impact had a FWHM of 1.6″, comparable to that of a point source, but with a low-level "wing" to the south of the brightest part of the impact site. The total spatial extent of the phenomena associated with the peak brightness of the G and K impacts subtended approximately 6″ and 6.6″ respectively above the 2.32–2.38 μm background tangent to the jovian limb. From the time the impact sites for G and K were first resolved, a 3.6″ radius aperture (G) and a 4.2″ radius aperture (K) were used to contain the majority of the light from the impact site as it rotated into view, while avoiding contamination from the nearby south polar haze. Poorer seeing on UT 18 July mandated a smaller aperture for the G impact to avoid scattered light from the polar haze, and typically there is 2–5% more light contained in a 4.2″ radius aperture, compared with a 3.6″ aperture. For both the G and K impacts, several points near the peak brightness of their main events have been corrected for changing effective telescope mirror aperture during the observations by comparison with total flux from the polar haze, which is assumed not to change throughout the impacts (cf. Section 2.2.3).

For the C, R, and W impacts, slightly smaller measurement apertures were used initially to avoid contamination from nearby old impact sites (A, G, and K, respectively), which were on or near the limb at the time of the impacts. Measurement apertures with radii in the range 0.9–1.8″ were used, and corrected to 3.6″ radius apertures for C and R. A smaller 3.0″ radius aperture was used for the W impact, which occured while the K impact site was on the limb. For the C and R impacts, aperture corrections were used throughout the entire impact sequence, even when the site became resolved, as a larger aperture would have contained contamination from the nearby older impact sites. As the W impact site rotated over the morning limb it became sufficiently separated from the older K impact site that it was possible to use a 3.6″ radius aperture after UT 8:18 (22 Jul).

2.3.2. Imaging data. The N and V impacts were much fainter than the six impacts observed with the spectral imaging technique, and were consequently more prone to contamination by the relatively bright scattered light from nearby impact sites. The photometrically reduced imaging data were further processed to minimize scattered light within the measurement aperture by subtracting a smoothed and averaged subset of the frames in each cube (after carefully "removing" any impact phenomena from these data) from each image in the data cube. A polygonal aperture was then used on these impact-site subtracted frames. The aperture is a 1.8″ × 1.4″ rectangle, with the lower 0.4″ × 0.4″ removed to minimize residual scattered light from the nearby impact site entering the measurement aperture. Running similar measurements on an imaging photometric standard star, we estimate that this aperture contains 60% of the light that would be contained in a 4.2″ radius circular aperture for a point source. Consequently the measured values were scaled to be equivalent to those measured through a 4.2″ circular aperture similar to those used for the spectral-mapping lightcurves.

2.4. Timing Estimates and Accuracy

All timing for the lightcurves was based on timestamp information recorded in the AAT data headers. The AAT timing standard is a quartz clock that keeps UT to within a few milliseconds. The VAX used to write the data and time stamp the headers has a clock that is not as accurate, but which is resynchronized to the UT clock once per day. There is also a difference between the recorded start time and the real start time for data taking, but this difference is only on the order of a few milliseconds. The largest potential source of timing error is found in the time stamping of the beginning and end of the IRIS exposure for each spectral-imaging datacube. This total time typically contains an extra 4 s above the astronomical exposure, which has been identified as a lag at the end of data-taking. This should not affect the time estimates as long as the start time is used as the reference time for calculating specific times for each scan step. Taking all the above factors into account, a conservative estimate would therefore

suggest that the timestamp information in the data headers is accurate to at least 1 s.

For the V impact sequence, which was taken as individual image frames, an average of the recorded start and end time for the exposure was used. For the N impact sequence the difference between the recorded start and end time was divided into 100 equal time segments for each of the 100 images within the cube.

For the spectral imaging data, which has two spatial (x, y) and one temporal (t) dimension, the lightcurve was measured first by extracting an image plane in the *yt* dimension for each of the observed datacubes. A centroiding program was then used to center on the impact phenomenon. The returned t position (which could have a fractional value) was multiplied by the scan step exposure time (usually 1.5 s per scan step) and added to the recorded start time (time $t = 0$) for the entire cube to produce a time for the impact phenomenon.

3. RESULTS

3.1. Timing and Lightcurves

Lightcurves for the impacts of C, D, G, K, R, and W are shown in Fig. 4. These lightcurves are extracted from the spectral-mapping datacubes in the wavelength range 2.32–2.38 μm to mimic the bandpass of the astronomical 2.34-μm CO filter used for our N and V imaging observations. This facilitates comparison of our spectral-mapping lightcurves with our 2.34-μm CO filter imaging observations, and similar imaging observations from other observatories. The CO filter imaging lightcurve for the N impact is shown in Fig. 5. No lightcurve is shown for the V impact, which was detected in only three successive imaging observations. However, the V image sequence is shown in Fig. 6.

We have determined significant timing events from these lightcurves, (e.g., detection of precursors and the main event, and the time of peak NIR brightness). However, we have used our spectral mapping data to also note the time that we first detected the onset of the sharp rise in intensity in our spectra near 2.295 μm due to the appearance of the CO 2–0 band. Illustrative spectra taken prior to and at the time of first CO detection for impacts C and K are provided in Fig. 7. A detailed description of the AAT spectral data and results will be provided in a subsequent paper (Meadows *et al.*, 2001, in prep). The impact event timings for fragments C, D, G, K, N, R, V, and W, including the time of first CO detection for all impacts for which we have spectra, are summarized in Table III.

3.1.1. Precursor phenomena. Each impact event was first detected as an unresolved point source on the morning limb of Jupiter near 45°S latitude. For the impacts of fragments C, D, G, K, N, and W, the brightest infrared flash was preceded by a faint precursor event. We did not detect a distinct precursor for the R impact, although comparison with data from the Keck, ANU 2.3 m, and Palomar observatories (Graham *et al.* 1995, McGregor *et al.* 1996, Nicholson 1996) suggests that this was due primarily to our sparse time sampling for this impact.

The precursor phenomena for G and K, two of the largest SL9 fragments, differ markedly from all other precursor phenomena we observed by displaying an underlying steady increase in brightness on which discrete precursor events are superimposed. Based on timing and intensity considerations, the precursors we observed for the impacts of C, D, and W are most likely to be second precursors; i.e., these phenomena are produced not by the incoming meteor trail, but are predominantly the signature of solid particles in the expanding impact fireball as it rises over the limb of Jupiter, and into view by ground-based telescopes. The precursor activity for G and K, however, probably also includes meteor activity that precedes the fragment impact.

We observed the precursors for fragments C and K with sampling times ranging from ~9 s to 1 min. Other precursor events (D, G, R, W) were observed with a 1- to 3-min sampling time, and in these cases, usually only a single point was recorded for each precursor.

Our fragment C precursor lightcurve was similar to that recorded by Takeuchi *et al.* (1995) at Okayama Observatory, and McGregor *et al.* (1996) at the Australian National University's 2.3-m telescope on Siding Spring Mountain. We first observed an unambiguous signal at 7:11:54 UT. This flash continued to brighten for 45 s, reaching a peak in our data at 7:12:38 UT. Observations from other observatories (ANU, Okayama) indicate that the precursor continued to brighten, peaking near 7:13:30 UT. Our next observation was taken at 7:15:26 UT, 3.5 min after initial detection, by which time the precursor had faded, dropping to preprecursor brightness levels. For this impact, comparison of absolute brightness levels between the three observatories is difficult, given the apparently differing fractions of the A impact site present in the chosen measurement apertures (the AAT data show a background of 0.08 Jy or 4.2×10^{-14} W m^{-2} μm^{-1} at 7:11 UT, compared with 0.45 Jy for the ANU and 1.2×10^{-13} W m^{-2} μm^{-1} for Okayama). At the peak of brightness in the subsequent main event, when the scattered light component would be negligible and a more accurate comparison could be made, both the ANU and Okayama observations were saturated. However, comparing values measured at 7:17:56 and 7:26:56 UT, the closest valid data points to the saturation limits that are common to all three observatories, flux values agree to within 10%, implying that differences in the brightness of the precursor event are probably due to different levels of jovian background radiation in the measurement aperture.

In our data, the D precursor was observed in a single observation, peaking at 11:54:42 UT before vanishing in the subsequent scan at 11:57:27 UT. Both AAT and ANU recorded 0.1 Jy for the peak flux of the D precursor. This was the faintest impact that we observed in spectral-imaging mode.

The time evolution of the fragment G precursor event did not show the brightening and fading behavior observed in the C and D precursors, but rather showed a predominantly increasing ramp of brightness up into the main event. Measured fluxes

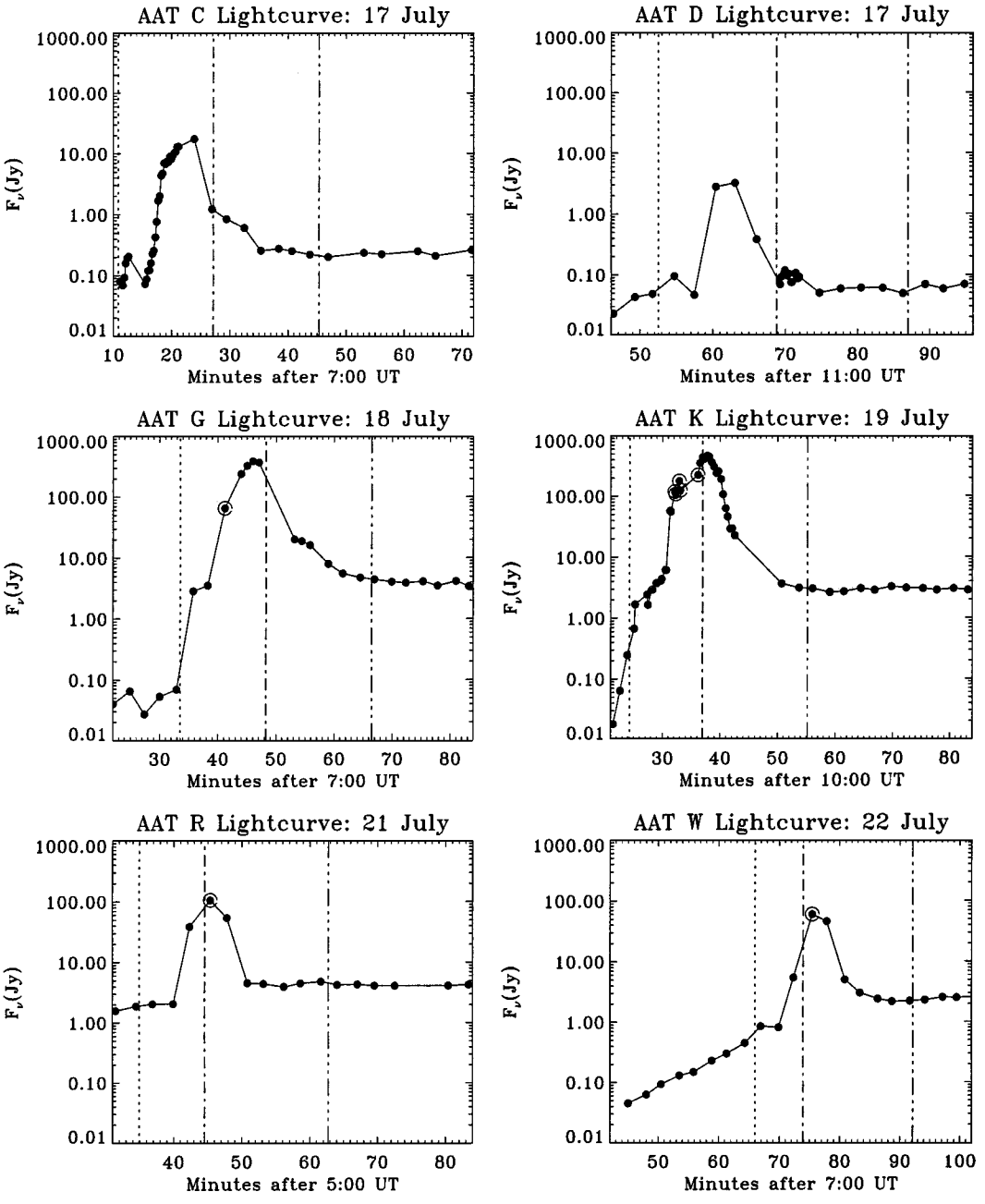

FIG. 4. Calibrated lightcurves. Diagram showing the time evolution of the C, D, G, K, R, and W impact events extracted from the spectral mapping cubes in the wavelength range 2.32–2.38 μm. The flux at each point is measured within a fixed aperture, regardless of whether the impact event is visible in the frame (see text for detailed discussion). The circled points indicate detector saturation. The dashed line indicates the accepted time of impact (Chodas and Yeomans 1996), the dot-dash line indicates the time at which the impact center rotated onto the morning limb of Jupiter and the dot-dot-dash line shows the time at which the impact center rotated into sunlight (the latter two times are calculated from the System III rotation rate and the meridian angle of the impacts from Table 5 of Chodas and Yeomans, 1996. Note that the meridian angle of the limb as viewed from Earth is 76°, and the meridian angle of the terminator is 87° (Chodas and Yeomans 1996)).

from the ANU and AAT agree to within 5% for this precursor. We first detected a point source at 07:32:55 UT at twice the brightness of the planet background. This "leader emission" preceded the first detection of this impact by the *Galileo* Photopolarimeter Radiometer (PPR) by 37 s (detection by PPR at 945 nm at 7:33:32 UT (Chapman *et al.* 1995a)). The *Galileo* Near-Infrared Mapping Spectrometer (NIMS) also detected an event at 7:33:37 UT (Carlson *et al.* 1995), 5 s after the PPR detection, and across a number of wavelengths from 0.7 to 5.3 μm. HST was also observing with an 889-nm filter at this time, and between 7:33:16 to 7:33:46 UT they clearly saw bright pixels in the shadow of Jupiter.

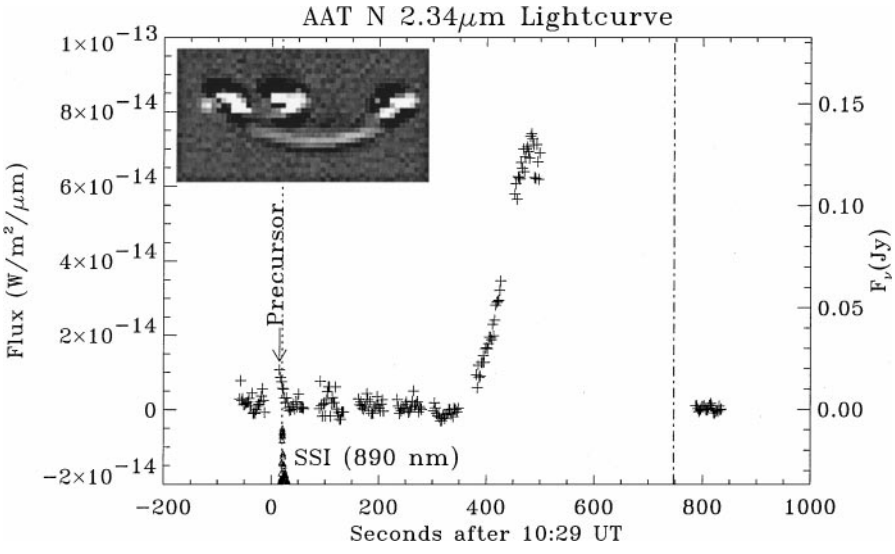

FIG. 5. The N impact light curve at 2.3 μm. Each cross is the sum of four 0.45-s exposures. The time of the precursor is labeled, and the inset image shows a disk subtracted image of Jupiter with the precursor on the morning (left) limb. The dark and bright patterns on the disk of Jupiter in this image are due to residuals after subtraction of the south polar cap and several previous impact sites. The dotted line shows the accepted time of impact. The dot-dash line shows the time that the impact center would have rotated onto the morning limb of Jupiter. The main event can be seen in the light curve between 380 and 500 s after UT 10:29:00. The gap in the lightcurve after this time was due to an instrument failure. The triangular symbols near the bottom of the plot show the timing of the flash observed by the Solid State Imager, on board the *Galileo* spacecraft. The intensity of the *Galileo* SSI data is not to scale.

In the next AAT scan at 7:35:47 UT, close to three minutes after our first detection, the point source had rapidly increased to ~50 times its initial value. Between 7:35:16 to 7:35:32 UT HST also detected an increase in source intensity compared to their previous 889-nm observation. A slight increase in this brightness by our next observation ~2.5 min later at 7:38:16 UT produced a sloping plateau in the lightcurve before the onset of the main event, which occurred sometime between 07:38:16 and 07:41:12 UT. From 7:38:16 to 7:38:32 UT, HST (at 953 nm) detected both the scattered light from the expanding plume, and what appeared to be thermal radiation along the angle of entry of the comet fragment (or exit of the plume). By their next observation at 7:41:16 UT, well into the upward slope of the main event lightcurve for the AAT, the HST detected an even larger plume.

The K precursor showed a structure similar to the G phenomena. For K, a faint point source was first detected on the morning limb at 10:22:38 UT, almost 100 s before the impact fireball was seen by the Solid State Imager (SSI) on board the *Galileo* spacecraft (SSI detection at 10:24:17 UT). The precursor's intensity increased by about a factor of 30 during the next 3 min (10:22:38 to 10:25:15 UT). The initial rapid rise in brightness slowed and the observed point source increased in brightness by only a factor of 3.5 over the next 5 min (until 10:30:39 UT), when it was overwhelmed by the main infrared flash. A similar 2.35-μm lightcurve was recorded by observers at ANU and Okayama. The Okayama results have higher time resolution over a longer time span than the ANU and AAT results and show a distinct, short-lived flash at 10:24:00 UT that they associate with the entry bolide (Takeuchi *et al.* 1995, Watanabe *et al.* 1995). It is interesting to note that in the AAT scan at 10:23:53 UT the precursor source appears to be extended away from the planet, but appears point-like on the scans on either side of this observation. However, this phenomenon could also be produced by scanning across a rapidly brightening point source. ANU does indeed show a rapid brightening in a frame that spans this time, and Okayama shows that the brightening peaks near 10:24:15 UT, which is almost simultaneous with the *Galileo* SSI flash detec-

TABLE III
AAT Impact Timing

Impact	Accepted (UT)	Precursor (UT)	Main event (UT)	IR max (UT)	Flux (Jy)	CO (UT)
C	07:10:50	07:11:39	07:16:45	07:24	17.5	7:24
D	11:52:30	11:54:46	11:57:27	12:03	3.23	12:06
G	07:33:33	07:32:58	07:38:19	07:46	385	7:45
K	10:24:17	10:22:42	10:31:18	10:38	466	10:36
N	10:29:20	≤10:29:14	10:35	10:37	0.14	—
R	05:34:57	05:34:00	05:42:22	05:45	106 (s)	5:47
V	04:23:20	04:23:13	—	04:23	0.02	—
W	08:06:00	08:06:56	08:12:20	08:15	60 (s)	08:18

Note. All times given are in UT. The accepted times for impact are from compilations by Chodas and Yeomans (1996). The precursor time quoted here is the very first detection of a point source on the jovian limb, and not necessarily the precursor peak. Column four gives the time of first detection of the IR main event, and column five gives the time of IR maximum from our data. The infrared flux values are the mean value in the bandpass between 2.32 and 2.38 μm. An "(s)" denotes the presence of detector saturation for the peak value, and is likely to be an underestimate of the true peak flux. The final column shows the time that hot CO line emission first becomes distinct from the underlying continuum at our sampling resolution (Meadows *et al.* 2001, in prep).

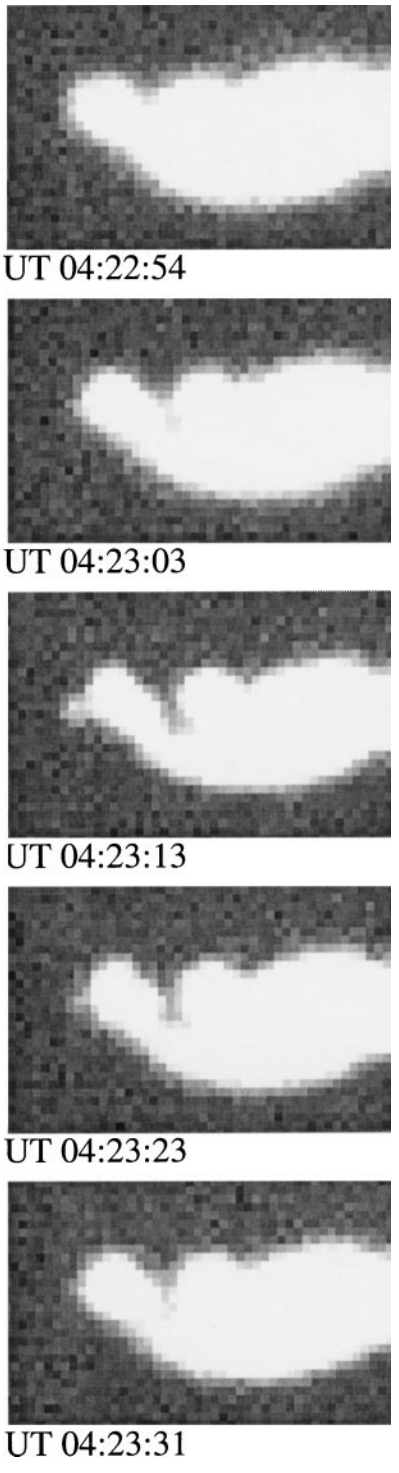

FIG. 6. V impact time sequence. Diagram showing the V impact flash at 2.3 μm. This series of images shows a section of the jovian disk that is dominated by the south polar haze and several old impact sites. The display range on these images has been adjusted to maximize the visibility of faint features. The V impact was first detected at 04:23:03 UT as several bright pixels off the morning limb of Jupiter (left on these images) at 45° latitude. By 4:23:13 UT, 10 s later, the impact had brightened and was an unmistakeable point source on the morning limb. It was seen fading at 4:23:23 UT and was undetectable 8 s later, at 4:23:31 UT.

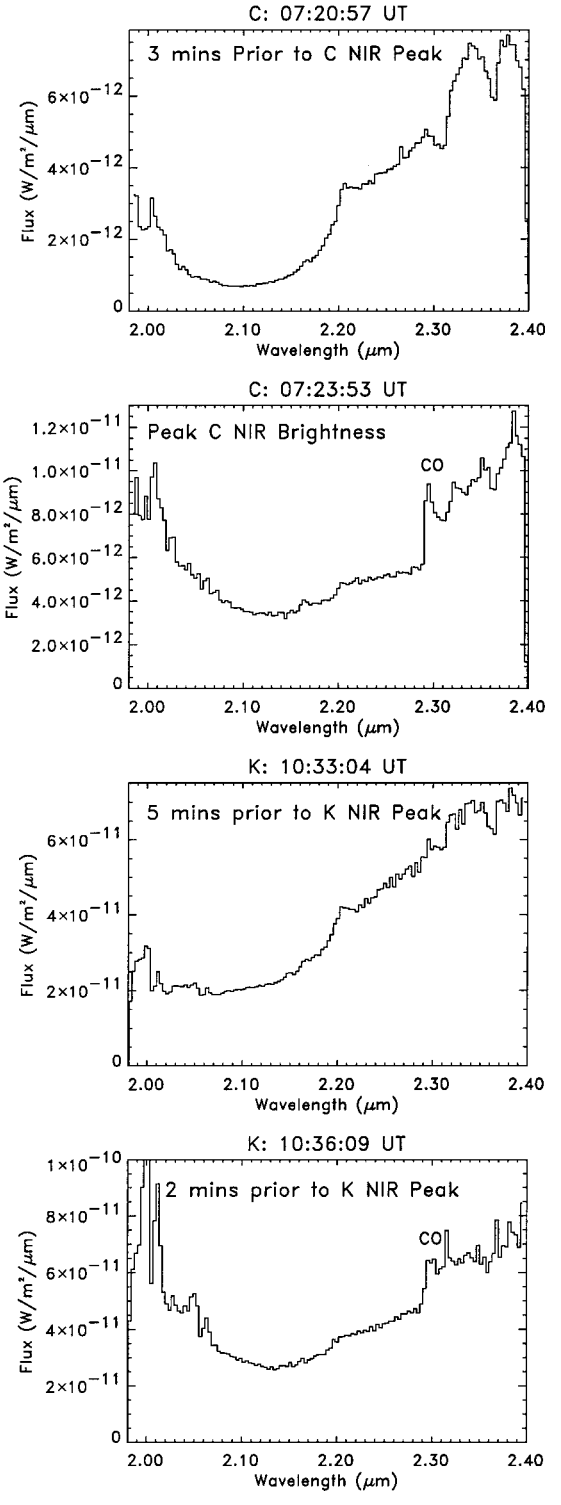

FIG. 7. Example spectra showing the onset of CO emission. These spectra are taken from the calibrated spectral mapping data used to produce the lightcurves for the C and K impacts. All spectra show the range 2.0–2.4 μm, and high-temperature CO emission was considered to be detected when we first saw the sharp rise of the CO 2–0 bandhead near 2.295 μm. The width and shape of this feature suggest CO at temperatures in excess of 1000 K. The top pair of spectra show the C impact just prior to and at the time of first CO detection, and the lower two spectra show the same sequence for the K impact.

tion (10:24:17 UT). The ANU and Okayama also both observed a sharp brightening near 10:25:30 UT and a subsequent decline. The peak of this feature was missed in our 10:25:15 UT observation, and the ensuing decline was missed in our subsequent 10:27:19 UT observation. Absolute flux values from all three observatories agree very closely (within 10%) for the duration of the precursor phenomena (10:20–10:30 UT). In addition to capturing the precursor phenomena for the K fragment impact by scanning across the jovian limb near 45° latitude, we had set the scan path up so that it would pass across the nearby satellite, Europa, which was in Jupiter's shadow at the time of the K fragment impact. It had been hoped that Europa would reflect the K fragment impact as a faint flash. However, we detected no such flash from Europa in our data.

After using the processing described in Section 2.3.2 to reduce scattered light from nearby impact sites, the N impact was first detected at 10:29:13 UT as a faint, but distinct, point source on the morning limb, which faded over the next 22 s. An image of the N precursor is shown in the upper left-hand corner of Fig. 5, and Fig. 8 shows a detailed plot of the precursor lightcurve. Our initial detection of this precursor was 4 s before the *Galileo* SSI detection of a sharp rise in brightness at 10:29:17 UT (which peaked 3 s later). The precursor we observed may have been present before 10:29:13 UT, as this was the first observation after a data gap that started at 10:28:48 UT. It is interesting to note that we detected a small rise in intensity on an otherwise monotonically decreasing first precursor at the same time that the *Galileo* SSI data recorded their peak brightness for this event. Although the AAT rise cannot be ruled out as noise in the data, if it is a real event it would imply that we saw the terminal event for N either directly, or scattered off dust from a tail behind the N fragment.

Models based on more extensively observed impacts (Chapman 1996) suggest that if this was indeed the first precursor for N, then it would have peaked about 8–10 s before the *Galileo* flash, or 4–6 s before we detected it at the AAT. For the other impacts observed by both *Galileo* and ground-based telescopes the time of the second precursor after the *Galileo* detection appears to be a function of distance from the limb of the impactor (Nicholson 1996). For the L and R impacts, which bracket the N impact, the second precursor was detected approximately 40 s after the *Galileo* detection. If the N impact behaved in a similar way, then the second, fireball precursor would have been started at 10:30:00 UT, and would have decayed over a period of 2 min.

However, at that time we have a data gap until 10:30:28 UT, after which the data are badly affected by variable seeing, which caused scattered light from nearby old impact sites to flare into the measurement aperture. The seeing is sufficiently poor that cancellation of light from nearby impact sites is also difficult, leaving large residuals in the data. By the next data block, which starts at 10:31:41 UT, the seeing had improved but a decaying second precursor was not detected. In fact, nothing as consistently bright as the first precursor is seen until the start of the main event at 10:35:20 UT. However, it may have been that this smaller impact produced a bolide that was far brighter than the subsequent fireball, which was certainly not the case for the impacts of larger fragments. However, like the AAT data, the *Galileo* SSI camera also detected a strong initial spike for the N event, which was attributed to the bolide flash in Jupiter's stratosphere (Chapman *et al.* 1995b), but the data showed little or no subsequent evidence for the fireball phase that followed the bolide flash in the larger impacts (e.g., K). They concluded, given that a main event was detected by ground-based observers, that the N fireball was below the detection limit for the SSI.

Given that the expanding fireball is linked physically to the generation of the splash phase, it seems more likely that second precursor brightness scales with the intensity of the subsequent main event, and not necessarily with the intensity of the bolide. For the other small impacts we observed (C and D) the second precursor peak was fainter than the main event peak by a factor of 30 to 90. If the N second precursor behaved in a similar way, then we would have expected its second precursor to reach a maximum peak of $2.5 \times 10^{-15}\,\mathrm{W\,m^{-2}\,\mu m^{-1}}$, which would have been undetectable in our data.

The R precursor was not observed as a distinct event in our data, due to our coarse time sampling.

The W precursor was detected in our data set as a single perturbation at 8:06:55 UT superimposed on a gradually increasing background as the old K impact site rotated into view over the morning limb of Jupiter. With higher temporal resolution, the ANU detected this precursor from 8:06 until 8:09 UT. At 8:06:16 UT HST first detected the W fragment impact as emission in shadow at 555 nm. This image was taken within 0.5 s of a 559-nm *Galileo* SSI image that is believed to show the incoming bolide (Chapman *et al.* 1995a). Our observation 39 s later was then clearly due to the expanding plume, and not the incoming bolide.

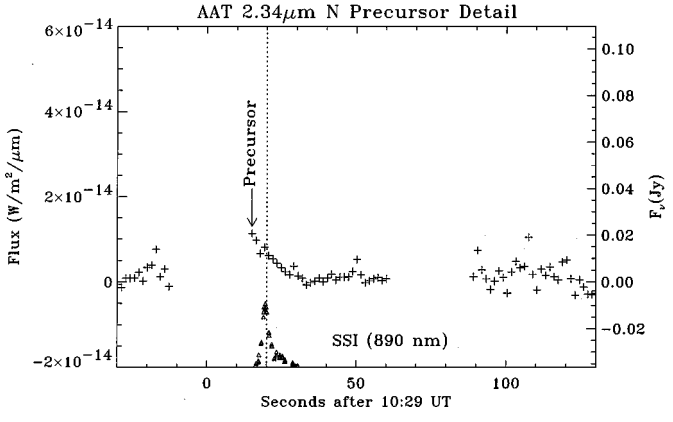

FIG. 8. The N impact lightcurve at 2.3 μm seen in detail. Each cross is the sum of three 0.45-s exposures. The time of the precursor is labeled. The dotted line shows the accepted time of impact (UT 10:29:20). The triangular symbols show the timing of the flash observed by the Solid State Imager, on board the *Galileo* spacecraft. The intensity of the *Galileo* SSI data is not to scale.

Comparison of the AAT and ANU measured fluxes for this second precursor are again complicated by the fraction of K impact site in the different measurement apertures used on each data set; nonetheless the difference between the background flux at 8:00 UT and the precursor value at 8:07 UT agrees to within 10%.

The impact of fragment V was detected only as one faint flash, seen in three consecutive images. A sequence of five IRIS images taken around the time of the V main event are shown in Fig. 6. Our detection peaked at 04:23:13 UT in observations that were 0.45 s long and separated by 6 s. A similar flash was observed at Palomar at 4:23:09 UT (Weinberger 1994, private communication; Nicholson 1996), consistent with our observations. The peak brightness of the flash, once scattered light from the nearby impact site was mitigated, was approximately 1.0×10^{-14} W m^{-2} μm^{-1} (0.02 Jy), although this value is highly uncertain (without the scattered light correction, the measured value is doubled). Either this flash could have been the main event for this impact, which would have been the brightest phenomena detectable for such a faint impact, or it could represent the first precursor (entry bolide) for this fragment. If the latter explanation is correct, then the fragment must have been destroyed on entry without producing a significant main event. The brightness of the detected event for V is comparable to the brightness of the first precursor detected for the N impact, which was also an "off-train" fragment of estimated size similar to that of V.

3.1.2. The main event. As observed in our data, and noted by other observers (McGregor *et al.* 1996), the main infrared flashes started approximately 5–6 min after the accepted impact time, irrespective of the distance from the limb, or the energy of the impactor. Of the impacts that we observed, fragments K and G produced the brightest infrared flashes and were presumably the most energetic impacts, followed by R, W, C, D, N, and V. Time measured from the beginning of the main event until peak infrared brightness did appear to be a function of impactor energy, with the most energetic impacts, G and K, taking 7–8 min to reach peak brightness, C, D, R, and W taking 4–5 min and the lowest energy impactor, N, taking 2 min. In our AAT spectral-mapping data, the first detection of CO emission above the continuum occurs within 11–13 min of the accepted impact time for all six impacts with spectroscopy. Because the CO appears at a fixed time relative to impact, but the main event peaks at a time that is a function of impactor energy, the CO appears at a different time relative to the main event peak brightness for different impacts. For the G and K events, CO was first detected prior to peak brightness. For C, D, R, and W it was detected after the peak of the main event, and so cannot be responsible for the main event peak value at 2.34 μm. Between 6 and 10 min after main event peak brightness, the intensities stabilized or increased slightly, forming a "shoulder" in the lightcurve. Prominent shoulders were observed for C, D, and G. At 6–10 min after peak brightness for the K impact, we switched to H-band observations and do not have K-band data for this time period. However, a shoulder was observed for the K impact during this time period by Okayama Observatory. For the impacts of R and W we acquired K-band data throughout the entire impact and did not record any obvious shoulder.

The C impact main event was first detected in our data at 7:15:56 UT. Over the next 8 min it increased in brightness by a factor of ~150 to peak at 7:23:53 at 17.5 Jy (9.6×10^{-12} W m^{-2} μm^{-1} at 2.34 μm). This peak value agrees well with the 1.0×10^{-11} W m^{-2} μm^{-1} peak recorded at the IRTF (Orton *et al.* 1995). Both ANU and Okayama saturated at the peak. However, the ANU data appear to record a higher value for the peak (~30 Jy), although the AAT and ANU data agree well for measurements taken well after the A impact site has cleared the limb. The next scan, taken at 7:26:56 UT, shows a 14 times decrease in intensity and the beginning of a broad shoulder that persists until 7:35:20 UT. Between 7:35:20 and 7:46:54 UT the impact site appears to brighten by ~10% and then fade again. While this change is probably within our measurement errors, there is evidence from ANU, Okayama, and IRTF that the C lightcurve reaches a minimum near 7:35 UT and increases slightly again. Similar behavior was observed in our D impact data (see below), but there are no ANU or Okayama data taken at this time that could corroborate this effect. In both instances, the impact site had rotated over the limb but was not yet in sunlight.

The D impact main event was first detected in our data as an extremely faint point source at 11:57:27 UT. By the next scan (12:00:26 UT) it had increased in brightness by nearly a factor of 100. It peaked in our data in the next scan (12:03:03 UT) at 3.23 Jy (or 1.77×10^{-12} W m^{-2} μm^{-1} at 2.34 μm). However, comparisons with the higher time resolution data from ANU indicate that we missed the peak, which occurred between 12:02 and 12:03 UT. The measured flux values at 12:03:03 for our data and the Okayama data agree within 2%. Okayama obtained observations closer to the peak that indicate that the maximum D brightness was probably close to 3.8 Jy. This is also consistent with the ANU peak brightness, despite the fact that their detector had entered its nonlinear response range. After peak brightness, the lightcurve decayed to a minimum at 12:09:17 UT, and a marked shoulder was observed between 12:09:27 and 12:14:42 UT. For the next 10 min the slow, low amplitude brightening and fading occurred as discussed in the previous paragraph.

The G impact main event started shortly after 7:38:16 UT and promptly saturated the detector. The AAT 3.9-m mirror was stopped down to 1.9 m diameter at this time while we continued observing. All subsequent data were unsaturated. The lightcurve reached a peak of 385 Jy at 7:46:00 UT. The ANU 2.3 m also recorded a maximum at this time, although their detector was in the nonlinear range and they measured close to 200 Jy. For a few minutes after 7:47 UT our data were lost or corrupted on transfer, and we resumed acquisition at 7:53:11 UT at the beginning of the shoulder phase of the lightcurve. At this time the AAT mirror was reopened to the full 3.9-m diameter. The shoulder had decayed by 8:01 UT, although the impact site continued to fade slowly with time.

The K impact main event started at 10:30:39 UT and IRIS saturated at 10:32 UT. We continued to acquire data but stopped the primary mirror down from 3.9 to 2.4 m diameter. After 10:36 UT, all data were unsaturated. We reached a peak in our lightcurve at 10:37:45 UT with a brightness of 466 Jy (2.55×10^{-10} W m^{-2} μm at 2.34 μm). Comparison of the calibrated data from AAT, ANU, and Okayama for this main event shows agreement to within 10% up until 10:32 UT, when a loss of signal due to saturation becomes evident in the ANU data, although the AAT (nominally saturated) data and the Okayama data continue in good agreement. However, by 10:36 UT the AAT is also clearly suffering from signal loss due to saturation, recording 30% less signal than Okayama. By 10:36:30, the AAT mirror was stopped down and the AAT and Okayama data agree again to within 10%. One apparent discrepancy however, is that ANU (albeit nonlinear) and the AAT both record a decrease in intensity between 10:38 and 10:39 UT, whereas Okayama saw an apparent increase. By 10:43 UT the main event intensity has faded and the shoulder starts forming in the Okayama data. At this point at the AAT we switched to acquiring H-band data, so the shoulder is missing from our 2.3-μm lightcurve. We resumed acquiring K-band scans of the impact site at 10:50 UT, shortly before it rotated into sunlight. As in the case for G, as the K impact point rotates into sunlight, there is no appreciable increase in the brightness of the impact site.

The N impact main event was first detected at 10:35:20 UT and it brightened rapidly, peaking in under 2 min to 0.14 Jy (7.5×10^{-14} W m^{-2} μm^{-1} at 2.34 μm) at 10:37:06 UT. This was 3.3×10^3 fainter than the K impact. Shortly after the peak we experienced a temporary instrument failure but resumed normal data taking at 10:42:06 UT, at which time the impact had faded and there was no sign of an impact site.

The R impact main event was first detected in our data at 5:42:19, when ANU and Keck data indicate that the main event was already 2 min old. Our peak flux of 106 Jy is detected at 5:45:21 UT. However, this value was taken within the nonlinear regime of our detector, and is likely to be an underestimate. The telescope was stopped down to 2.3 m after taking this measurement, so all subsequent points should not be affected by saturation. ANU and Keck also show a peak in measured radiation within seconds of our peak time, although ANU and Keck were also saturated at the peak. Although both ANU and AAT were saturated, they recorded a similar flux of close to 110 Jy, which although undoubtedly an underestimate, is still 30% higher than the peak flux reported by Keck observers (Graham *et al.* 1995), which was reconstructed from saturated data. After 5:51 UT there is slight evidence for a shoulder until 5:56 UT.

The W impact main event was first detected in our data at 8:12:20 UT, approximately 20 s after it was detected by ANU. Peak intensity of 60 Jy was observed at 8:15:25 UT. We saturated on the next scan and stopped the AAT mirror down to 2.0 m. Just prior to the peak, the ANU and AAT values are in good agreement; however, at the peak we are clearly saturated, recording a value 40% lower than that recorded by ANU, which was also saturating. The main event decreased rapidly in intensity from 8:17:49 until 8:20:49 UT, at which point it decreased more gradually, but in a curved dropoff, unlike the plateau-like behavior of a shoulder.

4. DISCUSSION OF LIGHTCURVES

Several authors have attributed the first distinct precursor to thermal emission from the meteor trail or "bolide" produced as the fragment or its attendant coma entered the jovian atmosphere (Chapman 1996). By analogy it is probable that the leader emission we observe for the larger impact fragments is a trail of dust or smaller fragments that precede the main fragment into the atmosphere. If this material impacted the atmosphere beyond the limb, it could be seen directly by Earth-based observers only if this emission was produced at sufficiently high altitudes that the tangent points were above the effective jovian limb.

The minimum emission and tangent altitudes at most infrared wavelengths are determined by the optical depth of the absorbing gases in the jovian atmosphere (CH_4, NH_3, and H_2). To estimate these altitudes we have ignored atmospheric refraction, which should introduce very small changes in apparent direction of the emitted radiation at pressures below 100 mbar, and used our line-by-line multiple-scattering model (Meadows and Crisp 1996) to produce high-resolution spectra of the gas and aerosol extinction in the jovian atmosphere.

Results from this model indicate that even though the broadband CH_4 opacity near 2.2 μm (and 3.5 μm) is consistent with a vertical optical depth unity near the 1-mbar level, this opacity is concentrated in narrow spectral lines that are separated by broad regions that are much more transparent. If the bolide flash consisted primarily of continuum emission, as our spectroscopic results suggest (Meadows *et al.* 2001, in prep), this emission could traverse much longer atmospheric paths at wavelengths within the far wings of the gas absorption lines where the gaseous absorption is much weaker. We find that the pressure of vertical optical depth unity in the far-wing regions between the strongest CH_4 lines is below the 100-mbar level.

For a tangent path on the jovian limb, the airmass is $\sim$40. At wavelengths within the more transparent regions of the far wings of the CH_4 lines, a limb path encounters optical depths near unity at tangent point pressures near 10–20 mbar ($\sim$90 km above the 1-bar level). Limb paths with larger tangent pressures encounter much more absorption because the optical depth in the far wings of spectral lines increases roughly as the square of pressure. In other words, at far-wing wavelengths where a limb path with a tangent altitude of 10 mbar encounters optical depths near unity, a path with a tangent altitude of 20 mbar will encounter path-integrated absorption optical depths near 4, and transmittances near e^{-4}, or $<$0.018.

These results suggest that ground-based observers can directly detect bolides on the far side of the jovian limb at wavelengths within strong CH_4 bands only if the minimum tangent altitude of the line-of-site path through the limb is greater than $\sim$90 km above the 1-bar level (Fig. 9). Hence, the bolide produced by

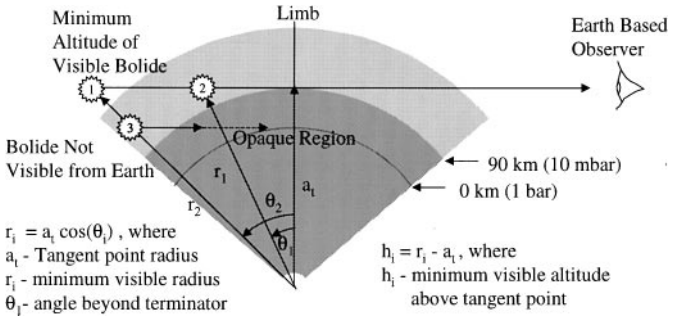

FIG. 9. This schematic diagram shows the derivation of the minimum altitude at which an SL9 fragment bolide would have been visible to ground-based observers. Optical depth unity within transparent regions between CH_4 absorption lines occurs near 90 km altitude (where the zero point of altitude is defined as the 1-bar level of the atmosphere). The opaque region of the atmosphere at lower altitudes and higher pressures is shown as the dark shaded region. To be visible to a ground-based observer, bolide 1, which occurred further beyond the limb, would have had to occur at a much higher altitude than bolide 2, so that its tangent path to the observer did not intersect the opaque region. As a specific example, the C fragment, which impacted 8° beyond the limb, would have been visible at an altitude of 790 km or above, whereas the W fragment, which impacted only 4° beyond the limb, would have been visible at altitudes of 260 km and above. However, bolide 3, which was the same angular distance from the limb, but deeper in the atmosphere than bolide 1, would not have been visible to a ground-based observer.

the C fragment, which enters the jovian atmosphere 8° beyond the limb, could be observed directly if it were produced at an altitude of at least ∼790 km above the 1-bar level, where the pressures are much less than 1 nanobar. Similarly, the bolide for the W fragment, which entered 4° beyond the limb, could be observed directly only if it were produced at least ∼260 km above the 1-bar level, at pressures near 30 μbars. It is unlikely that significant emission could be produced at these low pressures. These considerations suggest that it would have been virtually impossible to observe the fragment meteor trails directly for any of the impacts, especially the earlier impacts, which were further behind the limb.

However, the above calculations are for the fragment itself, which is surrounded by an extensive coma of dust. Although the comae became highly elongated along the Jupiter–SL9 direction just prior to impact (Weaver *et al.* 1995) the comae could still be seen extending several thousand kilometers in diameter perpendicular to the line of travel at visible wavelengths. In addition, for older comets undergoing breakup, e.g., Comet Encke, the infrared coma of larger particles far exceeds the extent of the visible coma, as larger particles remain around the nucleus and smaller particles are rapidly carried off into the Solar System, so that the small particles only trace the most recent production (Reach *et al.* 2000). Since SL9 was also clearly undergoing breakup, it is likely that a significant fraction of the coma extended beyond the visible extent seen in the HST pictures. Consequently, this large coma could have produced a rain of small meteors much closer to the jovian limb than the fragment itself. Given the above optical depth calculations, this would have significantly improved our chance of seeing this meteor activity directly from Earth.

This result alone strongly supports the theory put forward by Chapman (1996) that the first precursor is dominated by meteor showers generated by coma dust, rather than the bolide produced by the fragment itself. However, in addition, our spectroscopic evidence of the first precursors for several of the impacts (Meadows *et al.* 2001, in prep) clearly shows that this phenomenon was dominated by continuum emission from a source that was not subject to the long atmospheric path length implied by the minimum tangent altitude. Consequently, whatever was producing the emission during the first precursor stage must have been sufficiently close to the limb that it did not suffer a high degree of atmospheric absorption, further supporting the idea that the first precursor seen by ground-based observers was generated by coma dust falling closer to the limb, and not by the fragment itself.

Coma dust is also the most likely explanation for the "leader emission" seen prior to and several minutes after impact for the larger fragments. HST images of the Q2 fragment (Weaver *et al.* 1995), of estimated size comparable to that of the G and K fragments, shows an elongated trail of dust preceding and trailing the Q2 fragment two days prior to impact that has a spatial extent of tens of thousands of kilometers. The shorter leading trail and longer following trail imply coma impact times of 3 min before fragment impact and up to 16 min after impact, consistent with the observed leader emission, which was seen to start 1.5 to 3.5 min before the impacts of fragments G and K, and continue for at least 6 min after impact, before the signal was overwhelmed by the impact ejecta landing on the jovian atmosphere.

As seen in our lightcurves for C, D, G, K, N, R, and W, and noted by other observers (McGregor *et al.* 1996, Nicholson 1996) the main infrared flash started 5 to 7 min after impact irrespective of impactor energy (e.g., N was ∼3300 times fainter than K, but had a main event onset time within one minute of K's). The time to first detection of strong CO emitting at temperatures above 1000 K was also relatively independent of impactor energy, occuring between 11 and 13 min after impact for all impacts for which we had spectral information (C, D, G, K, R, and W). It is likely that these "fixed-time" impactor energy-independent phenomena are dictated by the flight time of the minimum vertical velocity required to produce the phenomenon that we recognize as the main event (Zahnle postulates that this is the production of the organic material seen as the dark cresent ejecta in HST images; Zahnle 1996; Hammel *et al.* 1995, 1996). Similarly the detection of CO at temperatures above 1000 K occurs at a fixed time after impact, corresponding to the energy generated by material with the minimum vertical velocity produced after 11–13 minutes of flight time.

However, unlike these two phenomena, the time to peak flux from the main event start is found to be a strong function of impactor energy, with times from lowest to highest energy

impactors (N to K) taking from 2 to 8 min to reach peak flux after the onset of the main event.

The brightness of the main event is a function of two main physical factors (as opposed to geometric viewing angle effects). These factors are the temperature that the ejecta is shocked to on impact, with hotter material producing correspondingly higher emission rates per amount of material, and the total amount of ejected material emitting. The peak brightness will correspond to the combination of the temperature of ejecta and the total bulk of ejecta landing.

For example, even though the ballistic model and some observational data suggest that the temperature of the ejecta shock increases with time as we see material with a higher initial vertical velocity land after a correspondingly longer flight time (Zahnle 1996, Kim *et al.* 1999), the main event does not increase in brightness indefinitely as the temperature of the ejecta steadily increases, but rather declines in brightness after a peak because correspondingly smaller amounts of this high vertical velocity material were produced in the impact. Fragment N, being a relatively low-energy impactor, ejects material with a range of vertical velocities that is relatively low, and travels a correspondingly short distance before impact with the atmosphere. This range of velocities, however, has components above the main event threshold energy corresponding to a 6-min flight time, and we see the main event start, but peak 2 min later as the bulk of the material impacts with the atmosphere after a relatively short flight time. Material does fall after this peak, and with higher energies and correspondingly higher molecular excitation temperatures, but the total amount of material that is falling is small, and the main event decreases in brightness. For the high-energy K impact however, the range of vertical velocities for impact ejecta is large, exceeding that produced in the N impact, so that after the onset of the main event emission, material continues to fall for many minutes.

It should also be noted that because of the time dependence of the peak of the lightcurve at 2.34 μm based on impactor energy, and the fixed time to first detection of CO emitting at temperatures above 1000 K, the CO became prominent *after* peak brightness for C, D, R, and W, and *before* peak brightness for G and K. So although the CO emission was very strong in the 2.34-μm (CO!) filters used for the majority of lightcurve measurements, the appearance of the CO emission was not solely responsible for the peak in the 2.34-μm lightcurves.

Another interesting result of this multi-impact comparison study is the correlation between inferred impactor size, preimpact, and the energy of the subsequent observed impact. While the majority of the impactors produced impacts consistent with their preimpact brightnesses and inferred size, N and V, two "off train" fragments traveling away from the main train of the comet, produced anomalously low-energy impacts when compared to their on-train counterparts.

For example, D and N were given the same preimpact relative intensity and size (1.0 relative intensity and 1.0 relative size for both; Weaver *et al.* 1995), and yet the peak flux measured for the

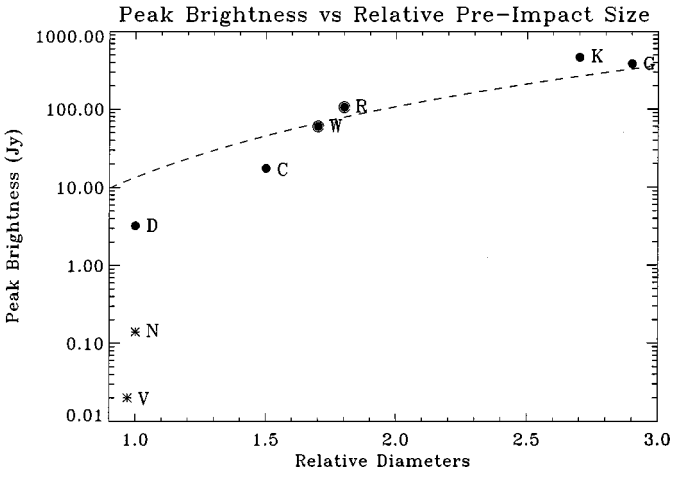

FIG. 10. Plot of peak brightness attained on impact at 2.3 μm *vs* the preimpact relative diameters assigned by Weaver *et al.* (1995). The circular symbols denote fragments on the main train. Ringed circles show peak brightnesses that were saturated, and so are likely to be lower than the actual value. The asterisks denote off-train fragment impacts. The dashed line shows a simple cubic relationship. (cf. Fig. 6 of Nicholson (1996)).

D impact was some 30 times higher than that observed for the N impact, implying that D was far more massive than N (Fig. 10). Weaver *et al.* also note that based on HST imaging, the off-train fragments generally produced ejecta patterns smaller than their pre-impact brightness would predict. If the relative sizes were indeed the same, the discrepancy in lightcurve peak brightness implies compositional and/or density differences between the D and N fragments, with N being 30 times less dense than D. V, which was ascribed a preimpact brightness of 0.95 and a relative size of 0.97 (Weaver *et al.* 1995), produced an impact lightcurve that was a some 190 times fainter than D, and 7 times fainter than N, implying an even smaller, or less dense fragment than the N fragment. However, if the off-train fragments had more dust than the on-train fragments, then their observed intensities may have been enhanced, producing an overestimate of their mass relative to the on-train fragments (Weaver *et al.* 1995).

5. SUMMARY AND CONCLUSIONS

We have analyzed data obtained with the Anglo-Australian Telescope of the C, D, G, K, N, R, V, and W impacts. These observations spanned a wide range of impactor energies, with brightnesses at 2.34 μm ranging from 466 Jy (K) to 0.02 Jy (V). We observed precursors for all impacts except V and R. The R impact precursor was detected by other observatories, but was missed at the AAT due to our sparse time sampling.

Precursor phenomena for the extremes of impactor energy did not follow the "classical" first and second precursor pattern of many of the medium-energy impacts observed at other observatories. The precursor lightcurve for the high-energy G and K impacts was characterized by "leader emission," a gradual

brightening at wavelengths between 2.1 and 2.4 μm, which preceded and continued through the first and second precursors. This phenomenon was possibly caused by the infall of dust associated with the larger G and K fragments. The low-energy N fragment impact showed a first precursor, but the anticipated second precursor was not detected. This pattern was also seen by the *Galileo* spacecraft, and indicates that a disproportionately large part of the fragment's energy was expended in the bolide, when compared to other, larger impactors. For the extremely low-energy V impact we detected only one short-lived flash, which was observed simultaneously at Palomar by Weinberger and Nicholson (McGregor *et al.* 1996). This single flash was more consistent with a first precursor (meteor) than a main event (splashback) and may indicate that the V fragment was destroyed on entry into the jovian atmosphere, without creating an impact plume.

For all fragments observed other than V, the main event starts 5–6 min after impact, even for the N fragment impact, which was 3300 times fainter than the K fragment impact. The time to first detection of strong CO emitting at temperatures above 1000 K was also relatively independent of impactor energy, occuring between 11 and 13 minutes after impact for all impacts for which we had spectral information (C, D, G, K, R, and W). However, unlike these two phenomena, the time to peak flux from the main event start is found to be a strong function of impactor energy, with lowest to highest energy impactors (N to K) taking from 2 to 8 min to reach peak flux after the onset of the main event.

These observations imply that the onset of the main event and the onset of emission from hot CO are related to a fundamental impact phenomenon, such as threshold vertical velocities, and not to viewing geometry or the energy of the impactor. However, the time to peak brightness is more likely to be determined by the vertical velocity of the bulk of the material producing the emission and so could depend on impactor energy.

"Shoulders," a flattening of the dropoff in intensity of the lightcurve after peak flux, were observed in our data for C, D, and G. Due to observing anomalies, we missed the shoulders for K and N. R and W were observed against or very close to a previous impact site, and exhibited only weak shoulder behavior.

The peak energy detected in the lightcurves relative to the preimpact brightness of the fragments was roughly consistent for the impacts of fragments C, D, G, K, R, and W, the only exception being that K produced a higher peak energy than the brighter, larger G fragment. However, relative to preimpact brightness, the N and V impacts were anomalously faint, which could indicate significant density differences for these off-train fragments, relative to fragments in the main train.

ACKNOWLEDGMENTS

This work was performed at the Jet Propulsion Laboratory, California Institute of Technology, under a contract with the National Aeronautics and Space Administration. V.S.M. and D.C. gratefully acknowledge generous support for this work from the NASA SL9 Data Analysis Program and from the NASA Planetary Atmospheres Program. J.B. gratefully acknowledges the support of the Caltech Summer Undergraduate Research Fellowship program. We thank the Anglo-Australian Observatory and the AAT Time Allocation Committee for the generous allocation of Anglo-Australian Telescope time, and for the exceptional technical and observing support provided to us for these difficult and time-critical observations. In particular, we thank Dr. Stuart Lumsden, Steve Lee, Jonathan Pogson, and Frank Freeman for their support in running the telescope and supporting IRIS at all hours of the day and night during the run, and Steve Lee and Tony Farrell for useful discussions about the IRIS time stamping. Useful scientific discussions were held with Dr. Timothy Brooke, Dr. Diana Blaney, Dr. Philip Nicholson, Dr. Peter McGregor, and Dr. Kevin Zahnle. Finally, we thank Dr. David Allen (1946–1994) for participation in the planning of this campaign, and for numerous suggestions about the logistics of using IRIS for these time-critical observations. We lost David 3 days after the impact of fragment W, and we deeply regret that his failing health robbed him of the opportunity to participate in this unique and exciting observing campaign.

REFERENCES

Allen, D. A., J. R. Barton, M. G. Burton, H. Davies, T. J. Farrell, P. R. Gillingham, A. F. Lankshear, P. L. Lindner, D. J. Mayfield, V. S. Meadows, G. E. Schafer, K. Shortridge, J. Spyromilio, J. O. Straede, L. G. Waller, and D. L. Whittard 1993. IRIS: An infrared imager and spectrometer for the Anglo-Australian Telescope. *Proc. Astron. Soc. Aust.* **10**, 298–309.

Boslough, M., D. Crawford, A. Robinson, and T. Trucano 1994. Mass and penetration depth of Shoemaker-Levy 9 fragments from time-resolved photometry. *Geophys. Res. Lett.* **21**, 1555.

Boslough, M., D. Crawford, T. Trucano, and A. Robinson 1995. Numerical modelling of Shoemaker-Levy 9 impacts as a framework for interpreting observations. *Geophys. Res. Lett.* **22**, 1821.

Carlson, R. W., P. R. Weissman, M. Segura, J. Hui, W. D. Smythe, T. V. Johnson, K. H. Baines, P. Drossart, Th. Encrenaz, and F. E. Leader 1995. Galileo infrared observations of the Shoemaker-Levy 9 G impact fireball: A preliminary report. *Geophys. Res. Lett.* **22**, 1557–1560.

Carter, B., and V. S. Meadows 1995. Fainter southern JHK standards suitable for infrared arrays. *Mon. Not. R. Astron. Soc.* **276**, 734–738.

Chanover, N. J., D. M. Kuehn, D. Banfield, T. Momary, R. F. Beebe, K. H. Baines, P. D. Nicholson, A. A. Simon, and A. S. Murrell 1996. Absolute reflectivity spectra of Jupiter: 0.25–3.5 micrometers. *Icarus* **121**, 351–360.

Chapman, C., W. J. Merline, K. Klaasen, T. V. Johnson, C. Herrernan, M. J. S. Belton, A. P. Ingersoll, and the Galileo Imaging Team 1995a. Preliminary results of Galileo direct imaging of S-L 9 impacts. *Geophys. Res. Lett.* **22**, 1561–1564.

Chapman, C., W. J. Merline, K. Klaasen, T. V. Johnson, C. Herrernan, M. J. S. Belton, A. P. Ingersoll, and the Galileo Imaging Team 1995b. Galileo direct imaging of impacts, K, N and W. *Abstracts for IAU Colloquium 156*, 17.

Chapman, C., 1996. Galileo observations of the impacts. In *The Collision of Comet Shoemaker-Levy 9 and Jupiter* (K. Noll, H. A. Weaver, and P. D. Feldman, Eds.), pp. 121–132. Cambridge Univ. Press, Cambridge, UK.

Chodas, P. W., and D. K. Yeomans 1996. The orbital motion and impact circumstances of Comet Shoemaker-Levy 9. In *The Collision of Comet Shoemaker-Levy 9 and Jupiter* (K. Noll, H. A. Weaver, and P. D. Feldman, Eds.), pp. 1–30. Cambridge Univ. Press, Cambridge, UK.

Clarke, J. T., R. Prange, G. E. Ballester, J. Trauger, R. Evans, D. Rego, K. Stapelfeldt, W. Ip, J.-C. Gerard, H. Hammel, M. Ballav, L. Ben Jaffel, J.-L. Bertaux, D. Crisp, C. Emerich, W. Harris, M. Horanyi, S. Miller, A. Storrs, and H. Weaver 1995. HST far-ultraviolet imaging of Jupiter during the impacts of comet Shoemaker-Levy 9. *Science* **267**, 1302–1307.

Graham, J., I. De Pater, J. Jernigan, M. Liu, and M. Brown 1995. Keck telescope observations of the Comet P/Shoemaker-Levy 9 fragment R Jupiter collision. *Science* **267**, 1320.

Hammel, H. B. 1996. HST imaging of Jupiter shortly after each impact: Plumes and fresh sites. In *The Collision of Comet Shoemaker-Levy 9 and Jupiter* (K. Noll, H. A. Weaver, and P. D. Feldman, Eds.), pp. 111–120. Cambridge Univ. Press, Cambridge, UK.

Hammel, H. B., R. F. Beebe, A. P. Ingersoll, G. S. Orton, J. R. Mills, A. A. Simon, P. Chodas, J. T. Clarke, E. De Jong, T. E. Dowling, J. Harrington, L. F. Huber, E. Karkoschka, C. M. Santori, A. Toigo, D. Yeomans, and R. A. West 1995. HST imaging of atmospheric phenomena created by the impact of Comet Shoemaker-Levy 9. *Science* **267**, 1288–1296.

Kim, S. J., M. Ruiz, G. H. Rieke, M. J. Rieke, and K. Zahnle 1999. High temperatures in returning ejecta from the R impact of Comet SL9. *Icarus* **138**, 164–172.

McGregor, P. J., P. D. Nicholson, and M. G. Allen 1996. CASPIR observations of the collision of Comet Shoemaker-Levy 9 with Jupiter. *Icarus* **121**, 361–388.

Mac Low, M.-M. 1996. Entry and fireball models vs observations: What have we learned? In *The Collision of Comet Shoemaker-Levy 9 and Jupiter* (K. Noll, H. A. Weaver, and P. D. Feldman, Eds.), pp. 157–182. Cambridge Univ. Press, Cambridge, UK.

Martin, T. Z., G. S. Orton, L. D. Travis, L. K. Tamppari, and I. Claypool 1995. Observation of Shoemaker-Levy impacts bu the Galileo Photopolarimeter Radiometer. *Science* **268**, 1875–1879.

Meadows, V. S., and D. Crisp 1996. Ground-based near-infrared observations of the Venus night side: The thermal structure and water abundance near the surface. *J. Geophys. Res. Planets* **101**, 4595–4622.

Meadows, V., D. Crisp, J. Barnes, R. Beebe, and L. Huber 1998. Volume(s) SL9_0008–SL9_0012, NASA Planetary Data System.

Meadows, V., D. Crisp, G. Orton, T. Brooke, and J. Spencer 1995. AAT IRIS Observations of the SL9 impacts and initial fireball evolution. In *Proceedings of the European SL9/Jupiter Workshop* (R. West and H. Bohnhardt, Eds.), pp. 233–238. European Southern Observatory, Garching.

Nicholson, P. D. 1996. Earth-based observations of impact phenomena. In *The Collision of Comet Shoemaker-Levy 9 and Jupiter* (K. Noll, H. A. Weaver, and P. D. Feldman, Eds.), pp. 81–109. Cambridge Univ. Press, Cambridge, UK.

Orton, G. S. 1995. Comparison of Galileo SL9 impact observations. In *Proceedings of the European SL9/Jupiter Workshop* (R. West and H. Bohnhardt, Eds.), pp. 75–80. European Southern Observatory, Garching.

Orton, G., and 57 colleagues 1995. Collision of Comet Shoemaker-Levy 9 with Jupiter observed by the NASA Infrared Telescope Facility. *Science* **267**, 1277.

Reach, W. T., M. Sykes, D. Lien, and J. K. Davies 2000. The formation of Encke meteoroids and dust trail. *Icarus* **148**, 80–94.

Sill, G. T., and R. N. Clark 1982. Composition of the surfaces of the Galilean satellites. In *Satellites of Jupiter* (D. Morrison, Ed.), pp. 174–212. Univ. of Arizona Press, Tucson.

Takeuchi, S., H. Hasegawa, J. Watanabe, T. Yamashita, M. Abe, Y. Hirota, E. Nishihara, S. Okumura, and A. Mori 1995. Near-IR imaging observations of the cometary impact into Jupiter: Time variation of radiation from impacts of fragments C, D and K. *Geophys. Res. Lett.* **22**, 1581.

Watanabe, J., T. Yamashita, H. Hasegawa, S. Takeuchi, M. Abe, Y. Hirota, E. Nishihara, S. Okumura, and A. Mori 1995. Near-IR observation of cometary impacts to Jupiter: Brightness variation of the impact plume of Fragment K. *Publ. Astron. Soc. Japan* **47**, L21.

Weaver, H. A., and 20 Colleagues 1995. The Hubble Space Telescope (HST) observing campaign on Comet Shoemaker-Levy 9. *Science* **267**, 1282.

Wehrli, C. 1986. *World Climate Research Programme (WCRP) Publication Series* No. 7, WMO ITD-No. 149, pp. 119–126.

Zahnle, K. 1996. Dynamics and chemistry of the SL9 plumes. In *The Collision of Comet Shoemaker-Levy 9 and Jupiter* (K. Noll, H. A. Weaver, and P. D. Feldman, Eds.), pp.183–212. Cambridge Univ. Press, Cambridge, UK.